



BIOMEDICINE

Bioresorbable shape-adaptive structures for ultrasonic monitoring of deep-tissue homeostasis

Jiaqi Liu^{1†}, Najia Liu^{1†}, Yameng Xu^{2,3†}, Mingzheng Wu^{1†}, Haohui Zhang^{4†}, Yue Wang^{1,5}, Ying Yan³, Angela Hill⁶, Ruihao Song^{1,7}, Zijie Xu^{1,8}, Minsu Park⁹, Yunyun Wu¹, Joanna L. Ciatti^{1,8}, Jianyu Gu¹, Haiwen Luan¹, Yamin Zhang¹, Tianyu Yang¹, Hak-Young Ahn¹, Shupeng Li¹⁰, Wilson Z. Ray³, Colin K. Franz^{11,12,13}, Matthew R. MacEwan³, Yonggang Huang^{1,4,8,10}, Chet W. Hammill^{6*}, Heling Wang^{14,15*}, John A. Rogers^{1,5,8,10,16*}

Monitoring homeostasis is an essential aspect of obtaining pathophysiological insights for treating patients. Accurate, timely assessments of homeostatic dysregulation in deep tissues typically require expensive imaging techniques or invasive biopsies. We introduce a bioresorbable shape-adaptive materials structure that enables real-time monitoring of deep-tissue homeostasis using conventional ultrasound instruments. Collections of small bioresorbable metal disks distributed within thin, pH-responsive hydrogels, deployed by surgical implantation or syringe injection, allow ultrasound-based measurements of spatiotemporal changes in pH for early assessments of anastomotic leaks after gastrointestinal surgeries, and their bioresorption after a recovery period eliminates the need for surgical extraction. Demonstrations in small and large animal models illustrate capabilities in monitoring leakage from the small intestine, the stomach, and the pancreas.

Disruption of homeostasis represents a core feature of disease pathogenesis. Monitoring homeostasis at relevant anatomical sites thus provides essential physiological and pathological information crucial to early diagnosis before the onset of externally observable symptoms. Recent work has demonstrated the potential for use of bioelectronic devices in continuous, noninvasive detection of changes in parameters related to homeostasis, including blood pressure and flow (1, 2), temperature (1), extracellular fluid pH (3), blood glucose (4, 5), tissue oximetry (6), and cerebral interstitial fluid (7). Measurement modalities rely on optical (7–10), thermal (11–13), or radiofrequency (2, 14–16) signals of physiological processes. Attenuation in biological tissues limits the use of these mechanisms to shallow depths, sometimes up to the centimeter scale (17–22), which is insufficient for assessments of deep tissues. Approaches to monitoring homeostasis in deep tissues such as computed tomography (CT), x-ray imaging, or biopsies are often costly, invasive, and incompatible with continuous detection. In this context, advanced ultrasound imaging methods are of growing interest given their ease of use, wide availability, absence of radiation exposure, and capacity to probe to substantial depths (10 cm or more) (23) at high spatial resolution (a few

hundred micrometers) (24). Recent advances in functional ultrasound imaging indicate possibilities for monitoring physiological (25, 26) and microbiological dynamics (27, 28) in complex environments.

Materials and structural designs

Millimeter-scale bioresorbable materials structures introduced here enable real-time spatiotemporal measurements of perturbations of chemical or physical homeostatic parameters in shallow or deep tissue locations by conventional ultrasound imaging, offering specific clinically relevant uses in temporary patient monitoring (see supplementary text in the supplementary materials for a detailed discussion about monitoring homeostatic dysregulation). These bioresorbable, thin, and flexible implants incorporate symmetrically distributed collections of structures that generate strong contrast in ultrasound images embedded in a soft, shape-adaptive matrix material (Fig. 1A), referred to hereafter as a bioresorbable, shape-adaptive, ultrasound-readable materials structure (BioSUM). A circular ring feature serves as an anchor for suturing the device to adjacent tissues. The matrix (Fig. 1A, green color) undergoes well-defined dimensional changes upon interactions with the surrounding biofluid environment by amounts that depend on

a local parameter of interest. These transformations change the spacings between the ultrasonic indicators by magnitudes that can be quantitatively determined by imaging. The indicators consist of small disks of bioresorbable metals (e.g., Mg, Zn, Fe, W, or Mo) selected to maximize the acoustic impedance mismatch with the surroundings to ensure strong contrast in ultrasound images. The envisioned clinical use case is in postsurgical monitoring of patient status throughout a recovery period, after which resorption into the body by means of hydrolysis and natural metabolic reactions naturally eliminates the device, thereby bypassing the need for surgical extraction procedures (Fig. 1, B to D).

Homeostatic pH regulation is crucial for maintaining proper cellular and physiological functions. Perturbations may result from endogenous metabolic crises (e.g., acidosis or alkalosis) or exogenous events (e.g., surgical interventions or trauma). For example, leakage of gastrointestinal (GI) fluids secondary to anastomosis surgeries may cause considerable alterations in local pH homeostasis, with the potential to propagate throughout the peritoneal cavity, leading to organ dysfunctions and failures (29). Accurate monitoring of the pH in tissues surrounding the anastomotic site thus offers an opportunity for early detection of leakage with high sensitivity and specificity, to allow for therapeutic interventions that can reduce the morbidity and mortality of postoperative complications in GI surgeries [which range from 5 to 25%, depending on the sites of anastomosis (29)]. The absence of standard clinical approaches for assessments and the vague nature of patient symptoms in many cases pose additional challenges to early and accurate detection of anastomotic leakage (see supplementary text for details about the severity of these complications). In our proposed scheme, suturing one or more BioSUMs near the location of the anastomosis as the final step of the surgical procedure provides the basis for frequent monitoring through ultrasound imaging during a recovery period (see supplementary text and fig. S1 for an alternative approach to fixation that uses bioresorbable adhesives). The small dimensions of the devices, their thin geometries, and their soft, flexible mechanical properties provide an additional deployment option by way of syringe injection (Fig. 1E, fig. S2, and movie S1) to facilitate implantation

¹Querrey Simpson Institute for Bioelectronics, Northwestern University, Evanston, IL 60208, USA. ²The Institute of Materials Science and Engineering, Washington University in St. Louis, St. Louis, MO 63130, USA. ³Department of Neurosurgery, Washington University School of Medicine, St. Louis, MO 63110, USA. ⁴Department of Civil and Environmental Engineering, Northwestern University, Evanston, IL 60208, USA. ⁵Department of Biomedical Engineering, Northwestern University, Evanston, IL 60208, USA. ⁶Department of Surgery, Washington University School of Medicine, St. Louis, MO 63110, USA. ⁷Department of Chemical and Biological Engineering, Northwestern University, Evanston, IL 60208, USA. ⁸Department of Materials Science and Engineering, Northwestern University, Evanston, IL 60208, USA. ⁹Department of Polymer Science and Engineering, Dankook University, Yongin 16890, Republic of Korea. ¹⁰Department of Mechanical Engineering, Northwestern University, Evanston, IL 60208, USA. ¹¹Regenerative Neurorehabilitation Laboratory, Shirley Ryan AbilityLab, Chicago, IL 60611, USA. ¹²Department of Physical Medicine and Rehabilitation, Feinberg School of Medicine, Northwestern University, Chicago, IL 60611, USA. ¹³The Ken and Ruth Davee Department of Neurology, Feinberg School of Medicine, Northwestern University, Chicago, IL 60611, USA. ¹⁴Laboratory of Flexible Electronics Technology, Tsinghua University, Beijing 100084, China. ¹⁵Institute of Flexible Electronics Technology of THU Zhejiang, Jiaxing 314000, China. ¹⁶Department of Neurological Surgery, Feinberg School of Medicine, Northwestern University, Chicago, IL 60611, USA.

*Corresponding author. Email: hammill@gmail.com (C.W.H.); wangh12006@tsinghua.edu.cn (H.W.); jrogers@northwestern.edu (J.A.R.)

†These authors contributed equally to this work.

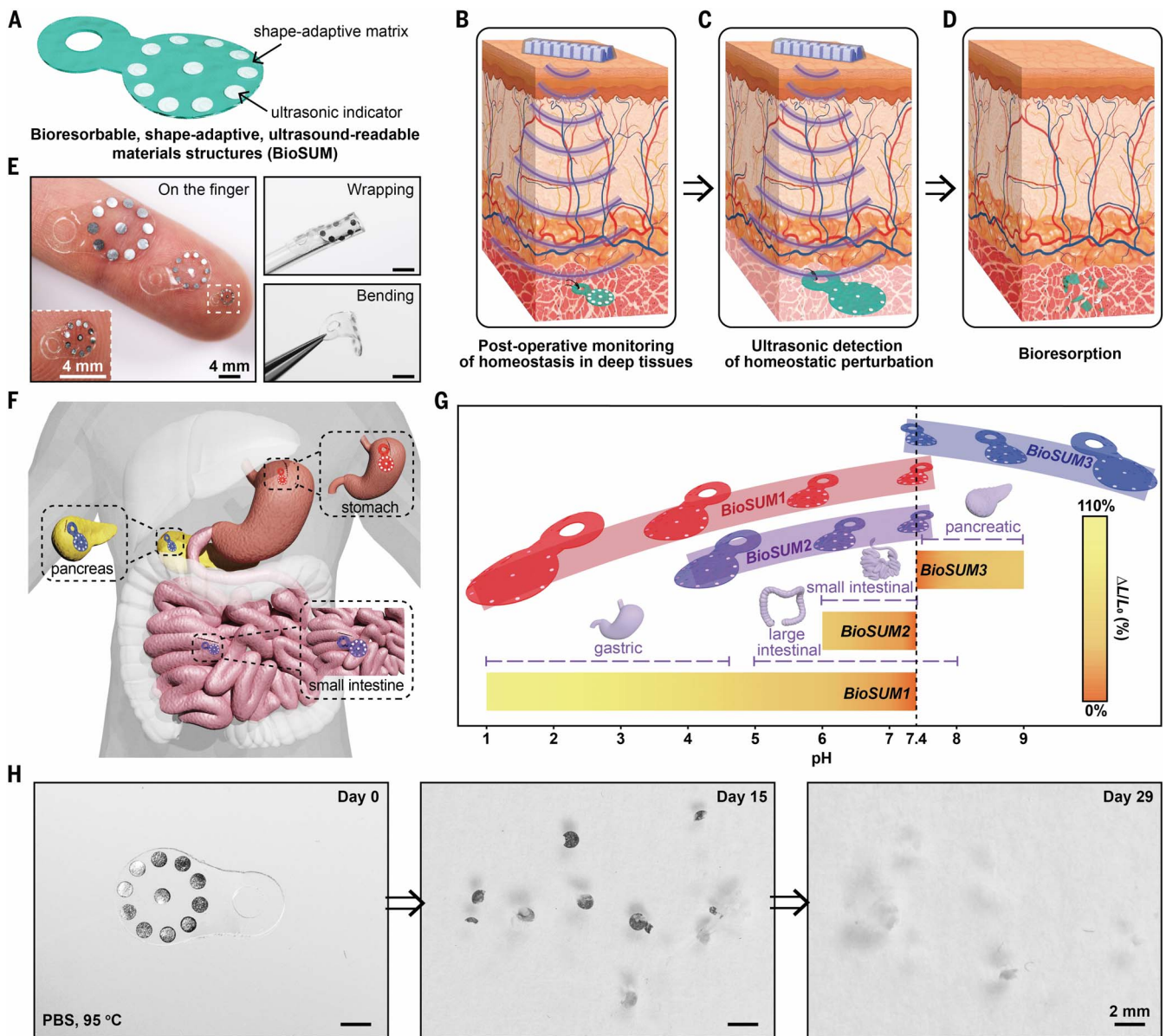


Fig. 1. Bioresorbable shape-adaptive ultrasound-readable materials structures (BioSUMs) for real-time monitoring of homeostasis in deep tissues. (A) Schematic illustration of our device, which includes a sparse collection of metal disks embedded in a thin hydrogel. (B) The BioSUM enables ultrasonic monitoring of homeostasis in deep tissues. (C) Ultrasonic signals from a BioSUM indicate homeostatic perturbations. (D) Subsequent bioresorption of the BioSUM eliminates the need for surgical extraction. (E) Miniaturized designs allow for implantation by laparoscopic surgery. Images

of three BioSUMs of different dimensions (12, 7, and 3 mm in diameter) on the finger (left), wrapped around a plastic tube with an outer diameter of 3.175 mm (top right), and in a bent state (bottom right). (F) Schematic illustration of a BioSUM for detecting postsurgical leakage from the stomach, small intestine, and pancreas. (G) pH-responsive ranges for BioSUM1, BioSUM2, and BioSUM3, and the corresponding pH values of representative digestive juices. (H) Images of the accelerated dissolution of a BioSUM2 in PBS (pH 7.4) solution at 95°C.

during laparoscopic surgeries (movie S2). Their bioresorbable construction eliminates the need for surgical extraction subsequent to a desired timeframe for operation. The examples presented here illustrate capabilities in monitoring gastric, small intestinal, and pancreatic leakage as three representative cases (Fig. 1F).

These illustrations rely on hydrogels as pH-responsive matrix materials, tailored to operate across relevant ranges of pH values. Specifically,

the gastric environment can present pH values as low as 1.0, thereby requiring hydrogels that swell in these acidic conditions while offering stable chemical and mechanical properties in these aggressive environments (BioSUM1). Monitoring for small intestinal leaks, by contrast, relies on hydrogels that operate at values of pH (~6.8) that are only slightly lower than normal physiological levels (~7.4) (BioSUM2). The pancreas presents alkaline conditions, thus requiring hy-

drogels that are responsive to pH values larger than 7.4 (BioSUM3). Figure 1G summarizes the relevant pH ranges for these three classes of hydrogels and their corresponding organ interfaces. Each is also designed to be fully bioresorbable (Fig. 1H and figs. S3 to S7; see supplementary text for the detailed mechanism). Choosing bioresorbable metals (30) and hydrogel materials (31–34) that undergo dissolution reactions and hydrolytic chain scissions in biofluids leads to

conversion into benign products over well-defined timescales. Figure 1H illustrates the accelerated dissolution pathway of BioSUM2 in phosphate-buffered saline (PBS; pH 7.4) at 95°C. The device largely dissolves within 15 days, and the residual materials disappear entirely after 29 days. At body temperature, the latter timescale corresponds to 174, 160, and 241 days for BioSUM1, BioSUM2, and BioSUM3, respectively.

pH-responsive behavior

The pH responses of the hydrogels originate from their chemical compositions. Materials for gastric and small intestinal leaks involve poly [2-(dimethylamino)ethyl methacrylate-co-2-(diisopropylamino)ethyl methacrylate] [p(DMAEMA-DPAEMA)] with polyethylene glycol diacrylate (PEGDA; number-average molecular weight $M_n = 250$) as a cross-linker (34, 35) (Fig. 2, A and B). DMAEMA and DPAEMA contain tertiary amine moieties that undergo protonation and subsequent changes in osmotic pressure as the pH decreases. The hydrogel chemistry that responds in alkaline conditions relies on poly (acrylic acid-butyl acrylate) [p(AAc-BA)] with PEGDA as a cross-linker (Fig. 2, A and C). Elevation of pH results in protonation of the carboxyl moieties in AAc and a corresponding conformational change of the hydrogel network due to hydrophilicity. Specifically, the addition of hydrophobic BA hinders the protonation of carboxyl groups around the original pK_a (where K_a is the acid dissociation constant) of the AAc moiety (~ 4.25) and shifts the swelling transition to values larger than the physiological pH of 7.4 (36) (see supplementary text, figs. S8 to S11, and tables S2 to S5 for details about materials designs). Finite element analysis (FEA) that includes the effects of coupled diffusion and deformation (37, 38) can capture the swelling kinetics in these polyelectrolyte hydrogels. Protonation of pH-responsive moieties enables the diffusion of buffer solutions into the cross-linked networks and successive expansion of elastomeric chains. The diffusivity (in the range of 10^{-8} to 10^{-12} m²/s) (37, 38) and the thicknesses of the hydrogels largely determine the swelling kinetics. The swelling ratio correlates to the inverse square of thickness, $\sim \tau/h^2$, where τ is time and h is thickness. Physical entanglement and grafted side chains in the hydrogel networks contribute to considerable swelling ratios at the equilibrium state (see supplementary text, figs. S12 to S14, and table S1 for more details about the swelling of hydrogels). FEA results predict the thickness-dependent swelling behavior of BioSUM1 for 10 min at different pH values, in terms of the percentage change in length ($\Delta L/L_0\%$) (fig. S15). To balance the need for both fast response time and small dimensions, the circular parts of the devices reported here have thicknesses of 300 μm and diameters of 7 mm, with a symmetrically distributed collection of thin, circular disks of Zn (1 mm diameter and

25 μm thickness) located at the midpoint of the thickness of the hydrogel (fig. S16A). The disks induce no measurable mechanical constraints on the swelling of the hydrogel matrix (fig. S17). Further miniaturized devices (4 mm diameter and 200 μm thickness), with expected enhancements in response times (figs. S16B and S18) facilitate use in small animal models.

Figure 2, D and E, presents experimental measurements and FEA results for the time-resolved swelling behavior of BioSUM1 in a citrate buffer solution at pH 4.5. Increasing the molar ratio of DPAEMA improves the mechanical robustness to ensure stable behavior in strongly acidic gastric fluids (figs. S9 and S19 to S21 and tables S2 to S4). This increase also, however, reduces the degree of swelling near physiological pH. Experimental measurements along with FEA modeling of the swelling ratios ($\Delta L/L_0\%$) for BioSUM1 and BioSUM2 are presented in Fig. 2, F to K. For example, BioSUM1 swells by 65% in pH 4.0 citrate buffer solution within 30 min, and BioSUM2 swells by 12% in pH 7.2 in the same timeframe. When in direct contact with simulated gastric fluid (SGF; pH ~ 1.2), BioSUM1 swells by 10% in less than 1 min and reaches $>35\%$ in 30 min (Fig. 2H). BioSUM2 can respond to 1 ml of simulated intestinal fluid (SIF; pH ~ 6.8) applied directly onto the device by swelling $>10\%$ within 10 min and $>15\%$ in 30 min (Fig. 2K). Figure 2, L and M, presents the response of BioSUM3 to alkaline conditions. BioSUM3 swells by 35% in pH 9 within 30 min (Fig. 2L), to an equilibrium swelling ratio of $\sim 40\%$ (Fig. 2M). BioSUM3 swells by 10% within 1 min after contact with 1 ml of simulated pancreatic juice (SPJ; pH ~ 8.2), and it reaches 30% in 30 min (Fig. 2N). FEA modeling accurately predicts the swelling kinetics for all cases (Fig. 2, F, I, and L).

Multiple devices at strategic anatomical locations relative to a surgical site provided the basis for spatiotemporal monitoring of the convective spread of SGF (Fig. 2, O and P, and figs. S22 and S23). Benchtop demonstrations involved the introduction of SGF on one end of a slab of agarose gel. Seven sensors distributed along a straight line in a thin layer of PBS solution on this gel allowed measurements of the swelling ratios at corresponding locations, to a distance of 30 cm from the origin at a spacing of 5 cm. Figure 2P shows the time-resolved responses of BioSUM1 at different locations, indicating expected performance and a spatial resolution comparable to the sizes and spacings of the devices.

Sensing by ultrasound imaging in deep tissues

Ultrasound B-mode imaging serves as a mechanism for quantitatively evaluating the pH-dependent geometry of these responsive hydrogels when implanted at deep tissue locations. The disks of Zn, an established bioresorbable metal that reacts with water to yield the benign end

product $\text{Zn}(\text{OH})_2$ (30), act as ultrasonic indicators. The acoustic impedance mismatch between these Zn structures and the surrounding hydrogel matrix and adjacent soft tissues enhances their visibility in B-mode images. The reflection coefficient is approximately proportional to $(Z_1 - Z_2)^2 / (Z_1 + Z_2)^2$ for structure thickness greater than ~ 20 μm for normal incidence specular reflections (39), where Z_1 and Z_2 are the impedances for the Zn and the hydrogel, respectively (see supplementary text and figs. S11 and S24 for details about reflections for thicknesses of <20 μm). For the systems reported here, the reflection coefficients at the interface between the Zn structures and the hydrogel are $>80\%$. By contrast, coefficients between typical surrounding soft tissues and the hydrogel are $<0.5\%$. The symmetric, circular distribution of these disks (Fig. 3, A to C) allows ultrasonic visualization in a manner that is independent of the orientation. During an ultrasound scan, acoustic waves generated by the transducer penetrate through tissues and reflect from these disks to form a cross-sectional image of their spacings. For the specific geometry presented here, the array of disks appears as three equally distributed bright segments in the image, clearly differentiated from background features associated with tissue structures. The distance between these hyperechoic components may shift in ultrasound images, depending on the specific cross-sectional position and orientation of the acoustic waves with respect to the device (Fig. 3A). The cross-sectional position across the diameter of the device represents the largest separation distance between bright segments in B-mode imaging, which defines the actual changes in dimension. An example of this process conducted in a rat model with a device on the surface of the stomach is shown in Fig. 3D. The left image denotes signals of BioSUM on the perimeter, and the right image shows signals from three disks along the diameter.

The symmetric design of the disks and the mechanically flexible nature of the BioSUM enable detection in nonplanar configurations (figs. S25 to S27). For example, when the BioSUM is not parallel to the transducer, it appears tilted in the B-mode image yet still reflects signals from the three disks along the diameter (Fig. 3C). The natural curvature of the targeted organs may lead to such tilted orientations (Fig. 3E) but without an effect on the measured distances between the disks, as in the right image of Fig. 3D. For additional details, see the supplementary text and figs. S28 and S29.

The signal-to-noise ratio (SNR) and the lateral resolution in B-mode images quantify the signal quality, yet both properties diminish with depth owing to the attenuation of ultrasonic waves as they propagate through the tissues. The lateral resolution (in terms of absolute length) is proportional to $\lambda F/L$ (40), where λ is the ultrasound wavelength, F is the focal depth, and

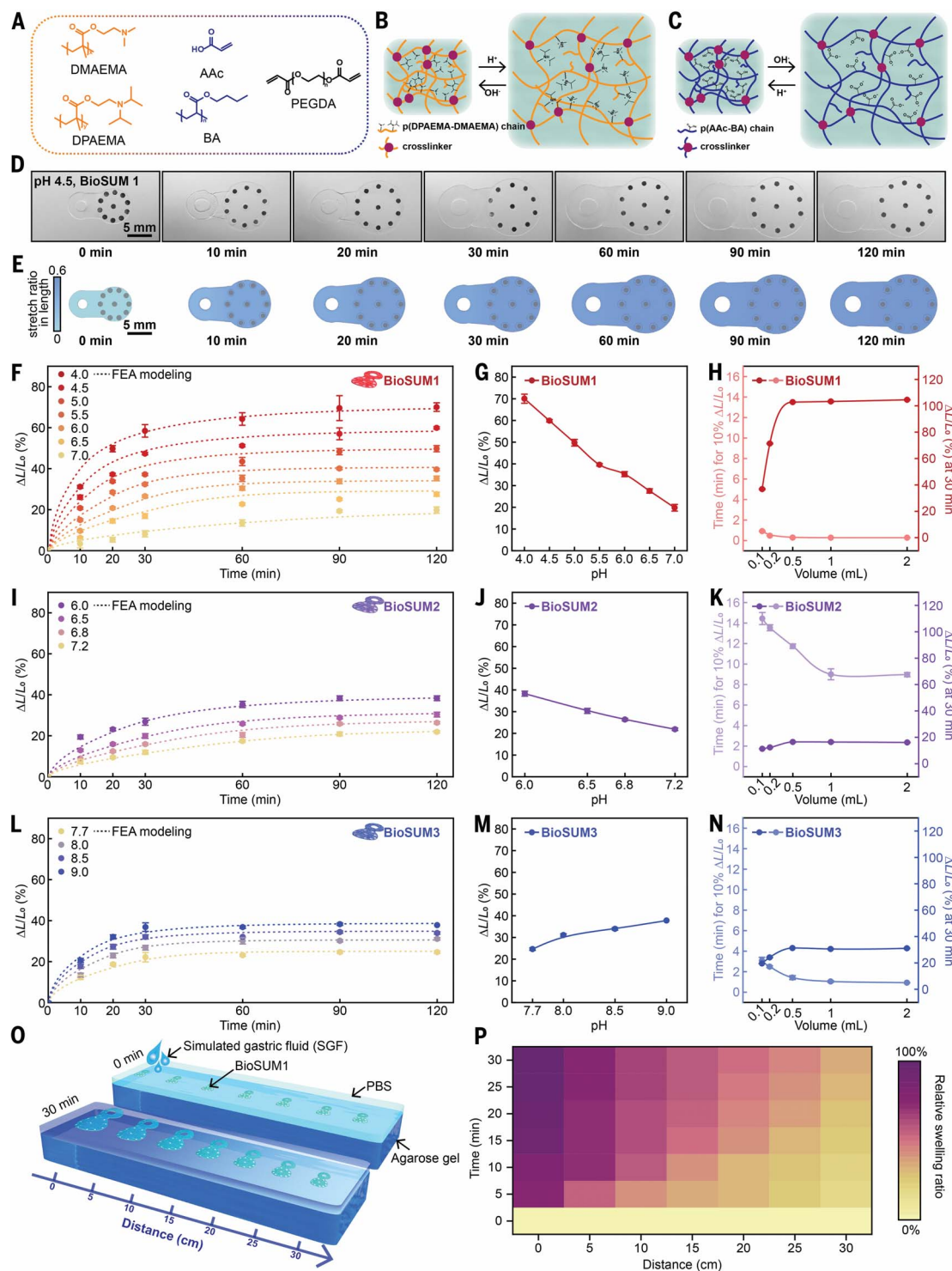


Fig. 2. pH-responsive behaviors of shape-adaptive materials structures.

(A) Chemical structures of the monomers, oligomers, and cross-linker in the pH-responsive hydrogels used in the BioSUM system. (B) Schematic illustration of the mechanism for pH-responsive hydrogels in BioSUM1 and BioSUM2. (C) Schematic illustration of the mechanism for the pH-responsive hydrogel in BioSUM3. (D) Time-dependent response of a BioSUM1 when immersed in a solution with pH 4.5. (E) FEA modeling results of the case shown in (D). (F, I, and L) Ultrasonic measurement of time-dependent responses of BioSUM1, BioSUM2, and BioSUM3, respectively, to immersion in solutions with different pH values. $\Delta L/L_0$ (%) denotes the swelling ratio. (G, J, and M) Response of BioSUM1, BioSUM2, and BioSUM3, respectively, to immersion

in solutions with different pH values at the equilibrium state. (H, K, and N) Optical measurement of sensitivity of a BioSUM to the introduction of different amounts of simulated GI fluids, including the response time for reaching 10% $\Delta L/L_0$ and $\Delta L/L_0$ at 30 min. (H) Response of a BioSUM1 to simulated gastric fluid. (K) Response of a BioSUM2 to simulated small intestinal fluid. (N) Response of a BioSUM3 to simulated pancreatic juice. (O) Schematic illustration of the setup for spatiotemporal mapping of pH with BioSUM1s. (P) Spatiotemporal characteristics, determined through optical methods, of BioSUM1s in response to the introduction of simulated gastric fluid at one end of the system. BioSUMs are fully swollen in PBS (pH 7.4) for 24 hours before the measurements presented here. Error bars in (F) to (N) represent \pm SD.

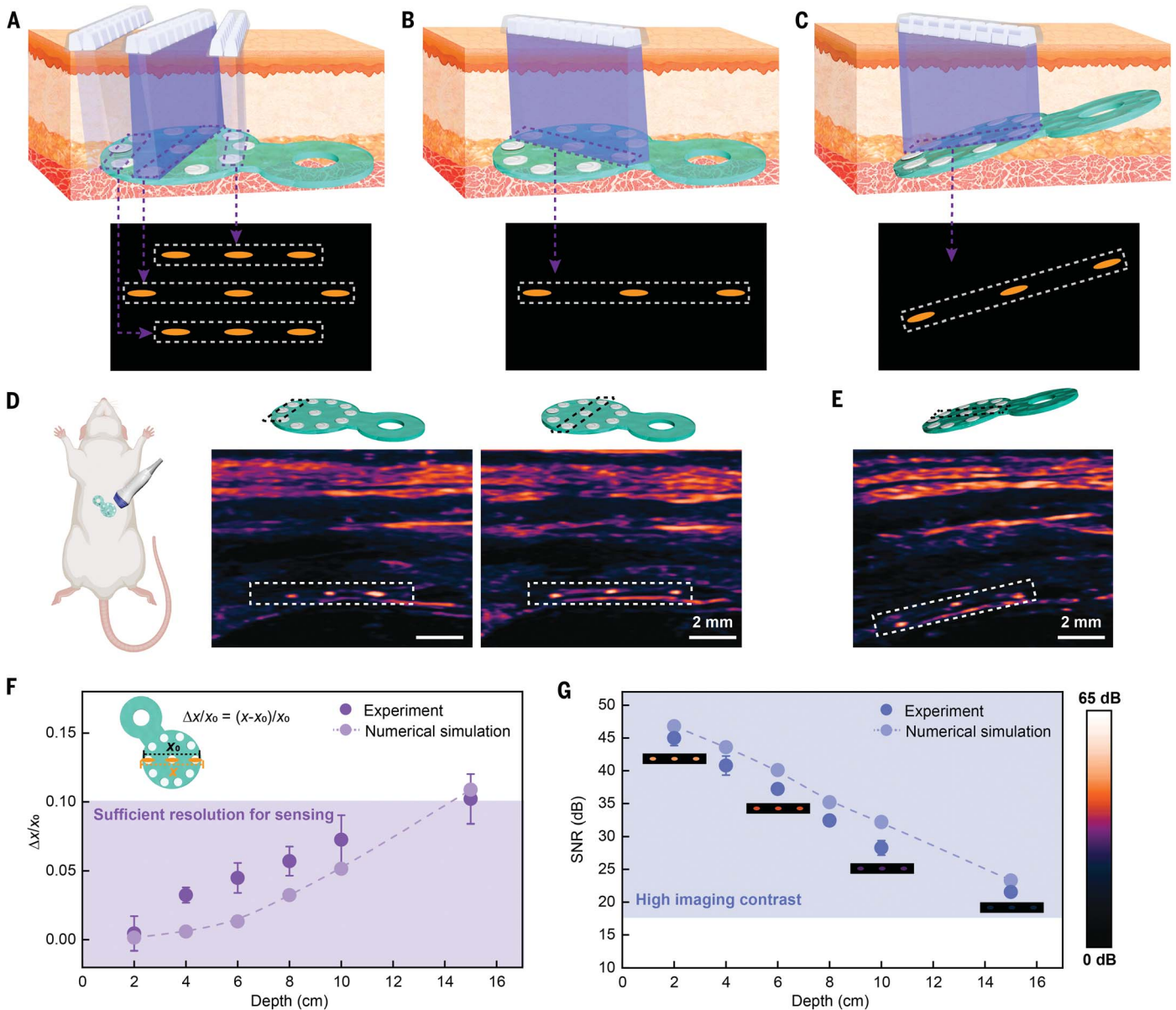


Fig. 3. Sensing by ultrasound imaging in deep tissues. (A) Schematic illustration of the cross-sectional position of acoustic waves relative to a BioSUM in different cases, and the corresponding signals in the ultrasound B-mode image. (B) The symmetric design enables ultrasonic visualization independent of the orientation of the transducer. (C) Schematic illustration of a BioSUM in a tilted case, and the corresponding signals in the ultrasound B-mode image. (D) Ultrasound B-mode images of a BioSUM on the stomach in a rat model demonstrating the cross-sectional position of acoustic waves in different cases,

correlated to the schematic illustration in (A). (E) Ultrasound B-mode image of a BioSUM in a tilted case on the stomach in a rat model, corresponding to the schematic illustration in (C). (F) Experimental and numerical simulation results for the measurement accuracy of a BioSUM at different depths. $\Delta x/x_0$ is the deviation of measured length divided by the actual length. (G) Experimental and numerical simulation results for the signal-to-noise ratio at different depths. Inset images are schematic illustrations of the image contrast in decibels. Error bars in (F) and (G) represent \pm SD.

L is the aperture length. With a fixed transducer (i.e., fixed aperture length) and scanning frequency (i.e., ultrasound wavelength), the resolution decreases with depth. Scattering from heterogeneous tissues causes attenuation that deteriorates the SNR as the depth increases. Experimental and numerical investigations (Fig. 3, F and G, and figs. S11 and S30 to S34) quantify the depth dependence of the signal quality using ultrasonic waves with frequencies of 5 MHz.

The experimental and numerical simulation results show similar trends over depth. The slightly lower signal quality from experiments may be attributed to effects of inhomogeneities in the soft tissues. The deviation of the measured separation between Zn disks divided by the actual separation, $\Delta x/x_0$, serves as a relevant metric. Numerical simulation and experimental results for images captured underneath a pork phantom in Fig. 3F show that $\Delta x/x_0$

increases with depth but remains <0.1 for depths up to 15 cm. This result indicates that dimensional changes of 10% or more can be accurately detected at depths of 15 cm, consistent with the swelling behaviors of the devices reported here. For SNR defined as the average contrast of three bright segments relative to the background, the results indicate that the SNR remains >18 dB for depths of up to 15 cm (Fig. 3G), which is necessary for clear visualization

Fig. 4. Longitudinal monitoring of pH homeostasis of the rat gastrointestinal system.

(A) Schematic illustration of the implantation and sensing procedure for a BioSUM1 on the stomach of a rat. [Created with Biorender.com]

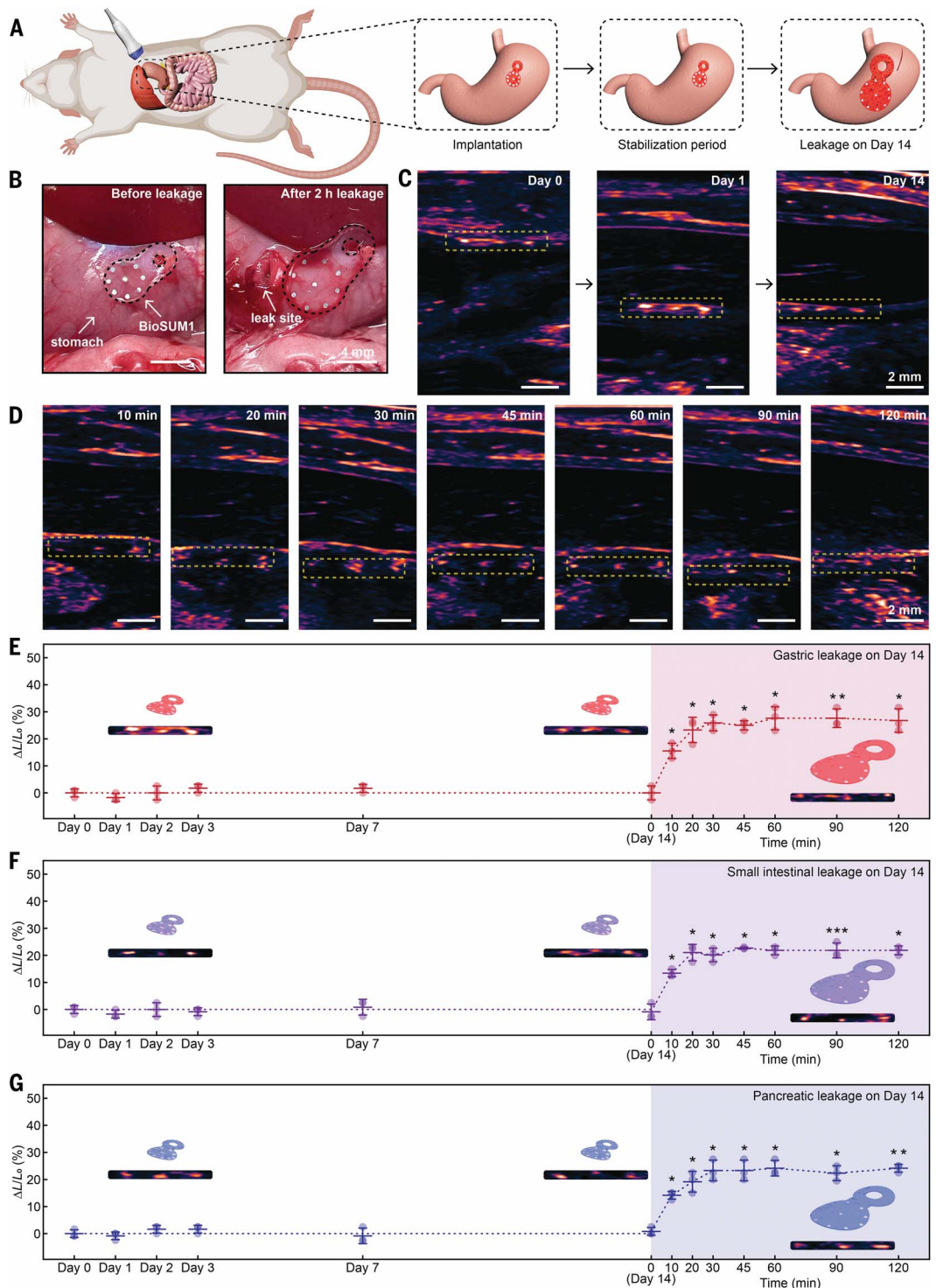
(B) Images showing the expansion of a BioSUM1 2 hours after creating a single gastrotomy. (C) Ultrasound images of a BioSUM1 on the stomach over a 14-day stabilization period without induced gastric leakage. The depth of the array of Zn disks changes between day 0 and day 1 because of postoperative relocation of organs.

(D) Longitudinal ultrasound images of BioSUM1 on the stomach after acute gastrotomy. (E) Summary data showing the swelling ratios of a BioSUM1 during the stabilization period and after acute gastrotomy. $n = 3$ biologically independent animals. Repeated measures (RM) one-way analysis of variance (ANOVA),

$P = 0.0008$, Holm-Sidak's multiple comparison test versus day 14 (0 min): 10 min, $P = 0.0208$; 20 min, $P = 0.0208$; 30 min, $P = 0.0198$; 45 min, $P = 0.0207$; 60 min, $P = 0.0208$; 90 min, $P = 0.0092$; and 120 min, $P = 0.0207$. Inset ultrasound images representing day 1, day 14, and 120 min were extracted from (C) and (D).

(F) Same as (E), but for a BioSUM2 and enterotomy. RM one-way ANOVA, $P = 0.0009$, Holm-Sidak's multiple comparison test versus day 14 (0 min): 10 min, $P = 0.0254$; 20 min, $P = 0.0254$; 30 min, $P = 0.0141$; 45 min, $P = 0.0254$; 60 min, $P = 0.0254$; 90 min, $P = 0.0005$; and 120 min, $P = 0.0254$. Inset ultrasound images representing day 1, day 14, and 120 min were extracted from fig. S43.

(G) Same as (E), but for a BioSUM3 and pancreatic leakage. RM one-way ANOVA, $P = 0.0021$, Holm-Sidak's multiple comparison test versus day 14 (0 min): 10 min, $P = 0.0231$; 20 min, $P = 0.0359$; 30 min, $P = 0.0359$; 45 min, $P = 0.0359$; 60 min, $P = 0.0348$; 90 min, $P = 0.0325$; and 120 min, $P = 0.0089$. Dots represent individual animals. Line represents B-spline. Error bars represent \pm SD. * $P < 0.05$, ** $P < 0.01$, *** $P < 0.001$. Inset ultrasound images representing day 1, day 14, and 120 min were extracted from fig. S44. BioSUMs were fully swollen in PBS (pH 7.4) for 24 hours before implantation, in all cases.



in medical imaging (23). The SNR and $\Delta x/x_0$ deteriorate as the diameter of the Zn disks decreases (figs. S11 and S30), as a limiting consideration in miniaturizing these structures. Simulation results indicate that to achieve $\Delta x/x_0 \sim 0.1$ and SNR ~ 18 dB, the hydrogel and

disks must have diameters of 3 and 0.5 mm, respectively (fig. S35).

Monitoring pH homeostasis in animal models

Longitudinal measurements using rat models validate the feasibility of ultrasonic detection

of GI leakage in a manner that is compatible with various ultrasound imaging systems (figs. S36 and S37). Our studies involved imaging after implantation on the stomach and for a subsequent 14 days to confirm the geometric and operational stability in this physiological

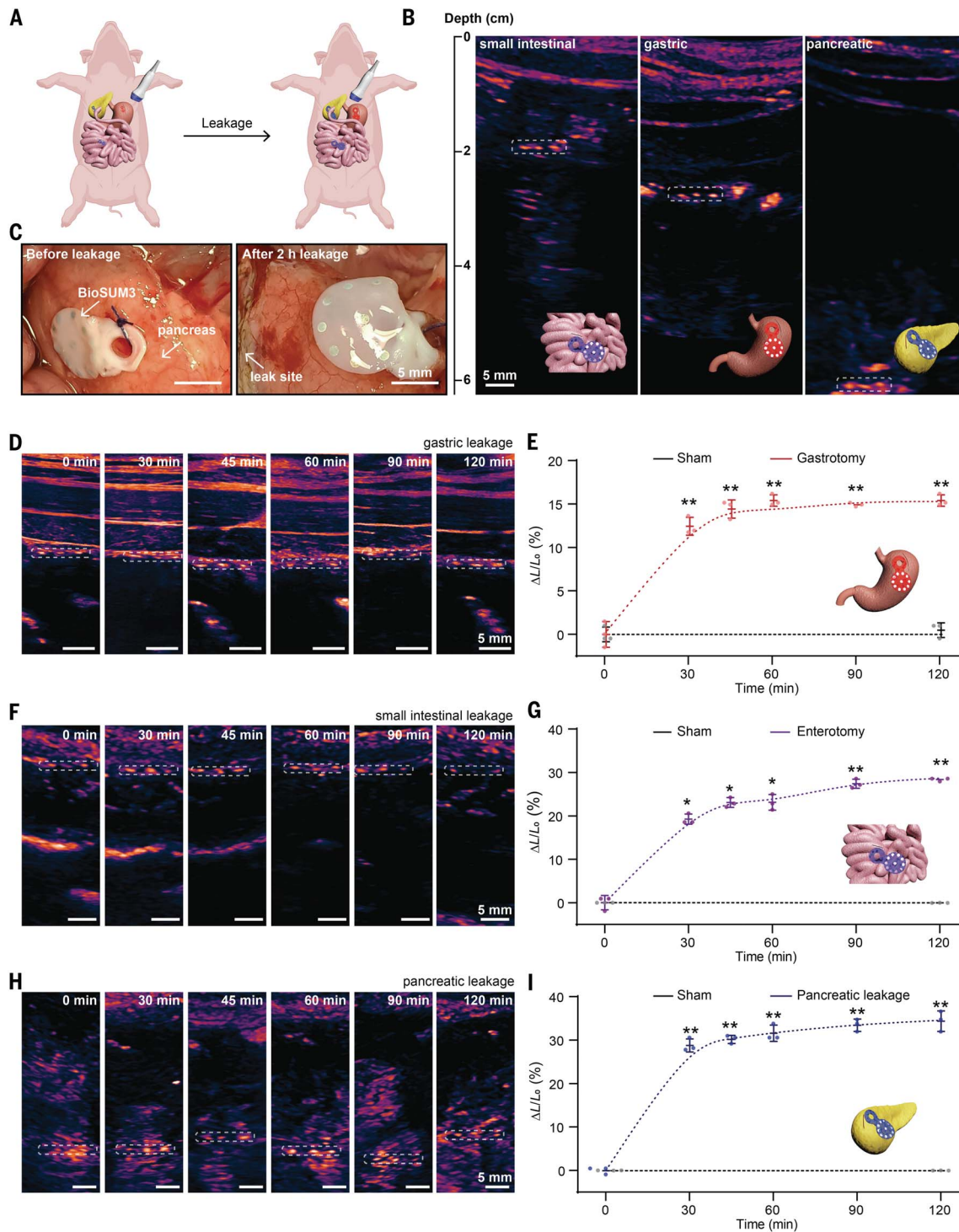


Fig. 5. Deep-tissue detection of gastrointestinal leaks in porcine models.

(A) Schematic illustration of the experimental procedures. [Created with Biorender.com] (B) Ultrasound images of BioSUMs on the small intestine (left, BioSUM2), stomach (middle, BioSUM1), and pancreas (right, BioSUM3) in a pig. (C) Images showing the expansion of a BioSUM3 after pancreatic leakage. (D) Longitudinal ultrasound images of a BioSUM1 after acute gastrotoomy. (E) Summary data showing the swelling ratio of a BioSUM1 with or without acute gastrotoomy. $n = 3$ independent samples per group. Two-way ANOVA, Holm-Sidak's multiple comparison with gastrotoomy $T = 0$ min: gastrotoomy, 30 min, $P = 0.0055$; 45 min, $P = 0.0024$; 60 min, $P = 0.0015$; 90 min, $P = 0.0019$; and 120 min, $P = 0.0024$; sham, 30 min, $P = 0.8568$. (F) Same as (D), but for a BioSUM2 and enterotomy. (G) Same

as (E), but for a BioSUM2 and enterotomy. $n = 3$ independent samples per group. Two-way ANOVA, Holm-Sidak's multiple comparison with enterotomy $T = 0$ min: enterotomy, 30 min, $P = 0.0351$; 45 min, $P = 0.0120$; 60 min, $P = 0.0120$; 90 min, $P = 0.0028$; and 120 min, $P = 0.0049$; sham, 30 min, $P = 0.9970$. (H) Same as (D), but for a BioSUM3 and pancreatic leakage. Dots represent individual samples. Line represents B-spline. Error bars represent \pm SD. * $P < 0.05$, ** $P < 0.01$. (I) Same as (E), but for a BioSUM3 and pancreatic leakage. $n = 3$ independent samples per group. Two-way ANOVA, Holm-Sidak's multiple comparison with pancreatic leakage $T = 0$ min: pancreatic leakage, 30 min, $P = 0.0045$; 45 min, $P = 0.0045$; 60 min, $P = 0.0045$; 90 min, $P = 0.0026$; and 120 min, $P = 0.0045$; sham, 30 min, $P = 0.9988$. BioSUMs were fully swollen in PBS (pH 7.4) for 24 hours before all the implantation procedures.

environment. Creating a 3-mm gastrotomy (incision in the stomach) on day 14 led to leakage, monitored immediately after closing the surgical site by imaging for a subsequent 2 hours (Fig. 4A and fig. S38). Visual inspection afterward confirmed the geometric changes (Fig. 4B). The results suggested minimal fluctuations in dimensions on postoperative days 1 through 14 (see supplementary text and fig. S39 for discussion on mechanical deformations), consistent with an absence of movement of the device and with a local pH stably maintained by homeostatic regulation (Fig. 4C and fig. S40). After the creation of a gastrotomy on postoperative day 14, the BioSUM1 expanded gradually during the 2-hour period, as evidenced by the increased distance between the Zn disks in B-mode images (Fig. 4D). The swelling was evident 10 min after the gastrotomy (Fig. 4E and fig. S41), even for the modest volume (<1 ml) of gastric fluid released in these experiments (4I). In addition, the expanded dimensions of the device after swelling remained stable after 2 hours. Further in vivo experiments confirmed this behavior for at least 6 hours after leakage terminated (fig. S42). Specifically, 2 hours after leakage ceased and the surgical site was closed, the rats moved freely for 6 hours. Ultrasonic evaluation after this period indicated that the dimensions were unchanged. In clinical practice, this behavior may prevent false-negative readouts that could otherwise arise as a result of delayed examinations. Similar procedures validated capabilities for ultrasound imaging of changes in pH associated with small intestinal and pancreatic leaks using the alternative hydrogel chemistries described previously (Fig. 4, F and G, and figs. S43 to S47). Real-time, dynamic changes in the pH of the local environment associated with leaks in the rat model obtained from benchtop studies of swelling behaviors are illustrated in fig. S48.

Tests on porcine models confirmed operation at scales comparable to the adult human GI tract (Fig. 5A). The results in Fig. 5B successfully demonstrate ultrasonic detection of BioSUMs on GI organs, imaged transabdominally through multiple layers of tissue with heterogeneous acoustic properties. Across this range of depths, the Zn disk array appeared as a distinct feature distinguishable from the background. Inducing GI leakage adjacent to the devices enabled monitoring of changes in a subsequent 2-hour period. Visual inspection confirmed these dimensional changes 2 hours after the creation of a pancreatic leak (Fig. 5C). The first ultrasonic scan, performed 30 min after creation of the GI leak, revealed significant dimensional changes in all three types of BioSUMs. The average swelling ratio was >10% at 30 min after the creation of the leak (Fig. 5, D to I). Histological analysis showed no remarkable inflammation, fibrosis, or necrosis compared with a sham group (figs. S49 and S50). Evaluations of blood chemistry indicated

results within normal ranges (fig. S51, A and B), and element analysis showed no significant accumulation of Zn in the heart, liver, spleen, lung, kidney, or blood, in comparison with the sham group (fig. S51C). In vitro cytocompatibility of BioSUMs revealed a negligible effect on cell viability and no significant cell death in close proximity to the devices (figs. S52 and S53).

Conclusions

We introduce bioresorbable shape-adaptive structures that enable rapid, noninvasive measurements of homeostasis in deep tissues by conventional ultrasound imaging techniques. The swelling of thin films of a responsive hydrogel matrix induced by homeostatic perturbations leads to changes in separations between sparse collections of bioresorbable metal elements functioning as indicators whose positions can be determined accurately by ultrasound. The large mismatch between the acoustic impedance of these elements and the surrounding materials produces high contrast in ultrasound images, thereby allowing for accurate measurements of their separations, and thus local physical or chemical characteristics of the surrounding tissues in shallow or deep locations. An envisioned clinical scenario is in real-time detection of anastomotic leakage through changes in pH during a period of recovery after a GI surgery, to allow for early intervention. The devices survive for a relevant timeframe and then naturally bioresorb, eliminating the need for secondary surgical extraction procedures. In vivo demonstrations of this concept in small and large animals validate materials designs tailored for use in gastric, small intestinal, and pancreatic leakage.

REFERENCES AND NOTES

1. K. Kwon *et al.*, *Nat. Biomed. Eng.* **7**, 1215–1228 (2023).
2. C. M. Boutry *et al.*, *Nat. Biomed. Eng.* **3**, 47–57 (2019).
3. M. Corsi *et al.*, *Adv. Sci.* **9**, e2202062 (2022).
4. L. Lipani *et al.*, *Nat. Nanotechnol.* **13**, 504–511 (2018).
5. Y. Chen *et al.*, *Sci. Adv.* **3**, e1701629 (2017).
6. H. Zhang *et al.*, *Sci. Adv.* **5**, eaaw0873 (2019).
7. J. Shin *et al.*, *Sci. Adv.* **5**, eaaw1899 (2019).
8. L. Lu *et al.*, *Proc. Natl. Acad. Sci. U.S.A.* **115**, E1374–E1383 (2018).
9. W. Bai *et al.*, *Nat. Biomed. Eng.* **3**, 644–654 (2019).
10. J. Kim *et al.*, *Sci. Adv.* **2**, e1600418 (2016).
11. K. Kwon *et al.*, *Nat. Electron.* **4**, 302–312 (2021).
12. R. C. Webb *et al.*, *Sci. Adv.* **1**, e1500701 (2015).
13. K. Kwon *et al.*, *Proc. Natl. Acad. Sci. U.S.A.* **118**, e2020398118 (2021).
14. S.-W. Hwang *et al.*, *Science* **337**, 1640–1644 (2012).
15. Y. S. Oh *et al.*, *Nat. Commun.* **12**, 5008 (2021).
16. D. R. Agrawal *et al.*, *Nat. Biomed. Eng.* **1**, 0043 (2017).
17. V. B. Koman *et al.*, *Nat. Nanotechnol.* **17**, 643–652 (2022).
18. S. Iwano *et al.*, *Science* **359**, 935–939 (2018).
19. S. Sonmezoglu, J. R. Fineman, E. Maltepe, M. M. Maharbiz, *Nat. Biotechnol.* **39**, 855–864 (2021).
20. S. Sharma *et al.*, *Nat. Electron.* **6**, 242–256 (2023).
21. A. Hai, V. C. Spanoudaki, B. B. Bartelle, A. Jasanoff, *Nat. Biomed. Eng.* **3**, 69–78 (2019).
22. V. Kalidasan *et al.*, *Nat. Biomed. Eng.* **5**, 1217–1227 (2021).
23. C. Wang *et al.*, *Nat. Biomed. Eng.* **5**, 749–758 (2021).
24. D. Maresca *et al.*, *Annu. Rev. Chem. Biomol. Eng.* **9**, 229–252 (2018).
25. E. Macé *et al.*, *Nat. Methods* **8**, 662–664 (2011).
26. A. Dizeux *et al.*, *Nat. Commun.* **10**, 1400 (2019).
27. R. W. Bourdeau *et al.*, *Nature* **553**, 86–90 (2018).

28. A. Farhadi, G. H. Ho, D. P. Sawyer, R. W. Bourdeau, M. G. Shapiro, *Science* **365**, 1469–1475 (2019).
29. E. Girard *et al.*, *J. Visc. Surg.* **151**, 441–450 (2014).
30. L. Yin *et al.*, *Adv. Funct. Mater.* **24**, 645–658 (2014).
31. A. Lendlein, A. M. Schmidt, R. Langer, *Proc. Natl. Acad. Sci. U.S.A.* **98**, 842–847 (2001).
32. S. S. Halacheva *et al.*, *Biomacromolecules* **15**, 1814–1827 (2014).
33. M. Changez, V. Koul, B. Krishna, A. K. Dinda, V. Choudhary, *Biomaterials* **25**, 139–146 (2004).
34. M. J. Bruining *et al.*, *Biomaterials* **21**, 595–604 (2000).
35. N. Deirram, C. Zhang, S. S. Kermaniyan, A. P. R. Johnston, G. K. Such, *Macromol. Rapid Commun.* **40**, e1800917 (2019).
36. O. E. Philippova, D. Hourdet, R. Audebert, A. R. Khokhlov, *Macromolecules* **30**, 8278–8285 (1997).
37. H. Zhang, M. Dehghany, Y. Hu, *J. Appl. Mech.* **87**, 061010 (2020).
38. W. Hong, X. Zhao, J. Zhou, Z. Suo, *J. Mech. Phys. Solids* **56**, 1779–1793 (2008).
39. N. M. Tole, *Basic Physics of Ultrasonographic Imaging* (World Health Organization, 2005).
40. J. T. Ylitalo, H. Ermer, *IEEE Trans. Ultrason. Ferroelectr. Freq. Control* **41**, 333–339 (1994).
41. E. L. McConnell, A. W. Basit, S. Murdan, *J. Pharm. Pharmacol.* **60**, 63–70 (2008).

ACKNOWLEDGMENTS

We thank S. Li, S. Papastefan, C. Redden, and J. B. Walters for preliminary efforts in testing. We thank Y. Gao and B. Jin for helpful discussions. Histology services were provided by the Northwestern University Research Histology and Phenotyping Laboratory, which is supported by NCI P30-CA060553 awarded to the Robert H. Lurie Comprehensive Cancer Center. Metal analysis was performed at the Northwestern University Quantitative Bio-element Imaging Center. In vitro cytocompatibility was supported by the Developmental Therapeutics Core at Northwestern University and the Robert H. Lurie Comprehensive Cancer Center support grant (NCI CA060553). We thank the Veterinary Diagnostic Laboratory at the University of Illinois Urbana-Champaign for conducting blood tests. This work made use of the MatCI facility supported by the MRSEC program of the National Science Foundation (DMR-1720139) at the Materials Research Center of Northwestern University. The schematic illustrations of the rat in Fig. 4A and the pig in Fig. 5A were created with BioRender.com. **Funding:** This work was funded by the Querry-Simpson Institute for Bioelectronics (J.L., N.L., M.W., Y.Wa., R.S., Z.X., M.P., Y.Wu, J.L.C., J.G., H.L., Y.Z., T.Y., H.-Y.A., and J.A.R.); the NSF Graduate Research Fellowship (grant DGE-2234667) (J.L.C.); the Washington University School of Medicine Surgical Oncology Basic Science and Translational Research Training Program grant T32CA009621 from the National Cancer Institute (NCI) (A.H.); the Belle Carnell Regenerative Neurorehabilitation Fund (C.K.F.); the Leadership in Entrepreneurial Acceleration Program (LEAP) at Washington University in St. Louis, Missouri (Y.X., Y.Y., W.Z.R., and M.R.M.); the National Natural Science Foundation of China (grant 12272352) (H.W.); and the Emerson Collective Cancer Research Fund (C.W.H.). **Author contributions:** Conceptualization: J.L., N.L., C.W.H., and J.A.R. Methodology: J.L., N.L., Y.X., M.W., Y.Y., C.W.H., and J.A.R. Theoretical simulations: H.Z., S.L., Y.H., and H.W. Investigation: J.L., N.L., Y.X., M.W., Y.Y., A.H., R.S., Z.X., M.P., Y.Wu, J.L.C., J.G., H.L., Y.Z., T.Y., H.-Y.A., W.Z.R., C.K.F., M.R.M., and C.W.H. Software: Y.Wa. Data analysis: J.L., N.L., Y.X., and M.W. Visualization: J.L., N.L., Y.X., and M.W. Supervision: C.W.H., H.W., and J.A.R. Writing – original draft: J.L., N.L., Y.X., M.W., H.Z., H.W., and J.A.R. Writing – review & editing: J.L., N.L., Y.X., M.W., H.Z., Y.H., C.W.H., H.W., and J.A.R. **Competing interests:** The authors declare that they have no competing interests. **Data and materials availability:** All data are available in the manuscript or the supplementary materials. **License information:** Copyright © 2024 the authors, some rights reserved; exclusive licensee American Association for the Advancement of Science. No claim to original US government works. <https://www.science.org/about/science-licenses-journal-article-reuse>

SUPPLEMENTARY MATERIALS

[science.org/doi/10.1126/science.adk9880](https://www.science.org/doi/10.1126/science.adk9880)
Materials and Methods
Supplementary Text
Figs. S1 to S53
Tables S1 to S5
References (42–76)
MDAR Reproducibility Checklist
Movies S1 and S2

Submitted 21 September 2023; accepted 12 January 2024
10.1126/science.adk9880